crystals

MDPI

Article

Ultrasonically Prepared Sodium Heparin-Stabilized Indocyanine Green/Nano-Hydroxyapatite Suspension for Collaborative Photodynamic and Photothermal Tumor Therapy

Qifa Song, Zi-You Ding, Chengyu Li, Yiran Fan, Xinli Tang and Yingchao Han *

State Key Laboratory of Advanced Technology for Materials Synthesis and Processing, Biomedical Materials and Engineering Research Center of Hubei Province, Wuhan University of Technology, Wuhan 430070, China
* Correspondence: hanyingchao@whut.edu.cn

Abstract: Indocyanine green (ICG) shows promise for diagnosing and treating tumors due to its good photothermal and fluorescent properties. In this study, sodium heparin (SH)-stabilized ICG/nano-hydroxyapatite (SH-ICG/nHAP) suspension was ultrasonically prepared to achieve photothermal and photodynamic collaborative therapy (PTT/PDT) for treating tumors. The nHAP had a short rod-like shape and a drug-loading capacity of 13.3% for ICG, corresponding to a drug-loading efficiency of 88.6%. In addition, the SH-ICG/nHAP suspension showed a very low release of ICG in PBS (7.4) and a slightly improved release in acidic buffers (6.5, 5.5), indicating an excellent binding ability of nHAP for ICG. The resulting SH-ICG/nHAP showed good suspension stability. Under an 808 nm near-infrared (NIR) laser, SH-ICG/nHAP showed good photothermal properties and could produce reactive oxygen species (ROS). Under the irradiation of an 808 nm NIR laser at 0.8 W/cm^2 for 5 min, SH-ICG/nHAP was found to significantly inhibit HepG2 cells proliferation (78.58%), similar to free ICG. *In vivo*, SH-ICG/nHAP was found to exert an improved inhibitory effect on tumor growth compared to free ICG. Biocompatible and stable SH-ICG/nHAP suspension like this could be a promising system for the PTT/PDT of tumors.

Keywords: ICG; nano-hydroxyapatite; suspension; PTT; PDT

Citation: Song, Q.; Ding, Z.-Y.; Li, C.; Fan, Y.; Tang, X.; Han, Y. Ultrasonically Prepared Sodium Heparin-Stabilized Indocyanine Green/Nano-Hydroxyapatite Suspension for Collaborative Photodynamic and Photothermal Tumor Therapy. *Crystals* **2023**, *13*, 1387. https://doi.org/10.3390/cryst13091387

Academic Editor: Rajratan Basu

Received: 27 August 2023
Revised: 11 September 2023
Accepted: 14 September 2023
Published: 18 September 2023

1. Introduction

Indocyanine green (ICG) is a near-infrared (NIR) optical material and fluorescent dye approved by the Food and Drug Administration (FDA) for clinical diagnosis [1–3]. ICG has reliable biological safety and excellent photothermal conversion capability [4,5]. ICG converts absorbed light energy into heat and produces excess ROS to inhibit the proliferation of tumor cells, allowing the photothermal or photodynamic treatment (PTT/PDT) of tumors [6]. In recent years, PTT/PDT has played an increasingly important role in the direction of tumor therapy [7]. An increasing number of studies have applied ICG to the collaborative therapy of tumors [5,8,9]. However, the use of ICG has shortcomings, such as poor stability, fast metabolism *in vivo*, and lack of targeting abilities [10–14]. These disadvantages greatly limit the efficacy of ICG *in vivo*.

Loading ICG into a suitable carrier is a potential method for solving the above problems. Nanocarriers have the advantages of a large specific surface area, long drug half-lives *in vivo*, and good targeting capabilities. At present, there are three main types of nanocarriers used in research: organic carriers (such as liposomes [15,16], polymers [17,18], micelles [19,20], and proteins [21]), inorganic carriers (such as calcium phosphate [22,23], gold [24,25], and mesoporous silica [26]), and hybrid-based carriers (such as mesoporous organosilica hybrids [27] and PEG-coated zinc oxide nanorods [28]). As the main component of teeth and bones, nano-hydroxyapatite ($Ca_{10}(PO_4)_6$ $(OH)_2$, nHAP) has good biocompatibility as a drug carrier [29]. Due to the abundant positively charged (Ca^{2+}) and negatively charged (PO_4^{3-}, OH^-) sites on its surface, nHAP has a good adsorption

ability for drugs, proteins, and genes [30,31]. Moreover, nHAP can be dissolved in an acidic environment; thus, nHAP can also be used as a pH-responsive drug carrier for controlled drug release [32,33]. In addition, nHAP exerts an inhibitory effect on cancer cells, including MGC-803 cells, Os-732 cells, and Bel-7402 cells [34]. Recently, several studies have been conducted on ICG-loaded nHAP that focus on their antitumor effects. Wang [35] prepared an L-Arg-modified mesoporous polydopamine-coated HAP nanocomposite to load ICG in for the ROS-triggered NO-enhanced PTT of tumor. Mushtaq [36] loaded ICG onto an Fe_4O_3-HAP nanocomposite and demonstrated the antitumor effect of the delivery system *in vitro*. Cheng [37] used polyacrylic acid (PAA) to disperse nHAP carriers to obtain glucose @HAP/ICG-NPs with good suspension stability, and the drug system played a good role in combined tumor therapy. Furthermore, Zhang [36,38] prepared a multifunctional nano-hydroxyapatite/MXene scaffold, and this scaffold can not only inhibit the proliferation of bone tumor cells under the 808 nm NIR irradiation, but also enhance osteogenic activity.

In this study, we designed a simple and effective approach to prepare sodium heparin (SH)-stabilized ICG/nHAP (SH-ICG/nHAP) suspension by using ultrasonic dispersion and SH stabilization effects. The effects of ultrasonication time and SH concentrations on the preparation of SH-ICG/nHAP were investigated. The morphology, phase composition, drug-loading capacity, particle size distribution, and stability of the materials were characterized. The antitumor effect of the SH-ICG/nHAP was evaluated both *in vitro* and *in vivo*. In addition, the biosafety of the SH-ICG/nHAP was evaluated.

2. Materials and Methods

2.1. Materials

Sodium phosphate ($NaHPO_4 \cdot 12H_2O$), calcium chloride ($CaCl_2 \cdot 2H_2O$), and 1,3-diphenylisobenzofuran (DPBF) were purchased from Aladdin. ICG (95%) and SH (150 UI/mg) were purchased from YuanYe (Shanghai, China). CCK-8 was purchased from HYCEZMBIO (Wuhan, China), Calcein-AM/PI was purchased from YEASEN (Shanghai, China), and DCFH-DA was purchased from Beyotime Biotechnology (Shanghai, China).

2.2. Preparation of nHAP

In this study, nHAP was synthesized by the hydrothermal method. Briefly, equal volumes of 0.05 mol/L $CaCl_2 \cdot 2H_2O$ and 0.03 mol/L $NaHPO_4 \cdot 12H_2O$ solution were mixed, and the pH was adjusted to 10.5. Then, the solution was placed in a high-temperature and high-pressure reaction kettle (180 °C, 3 Mpa, 8 h). Finally, the sample was centrifuged three times (7000 r/min, 5 min) by a centrifuge.

2.3. Preparation of SH-ICG/nHAP

First, the ICG was transferred into the prepared nHAP and stirred thoroughly in the dark for 2 h. Then, the SH was transferred into the ICG/nHAP. Finally, the SH-ICG/nHAP suspension was prepared using a previously described ultrasound-assisted method [39]. The ultrasound power is 200 W and ultrasound time is 8 min. The UV–vis absorption spectroscopy of ICG in the supernatant was recorded, and the drug-loading efficiency (DLE) and drug-loading capacity (DLC) were calculated according to the following formulas:

$$DLC(\%) = \frac{M_{loaded\ ICG}}{M_{nHAP}} \times 100\% \quad (1)$$

$$DLE(\%) = \frac{M_{loaded\ ICG}}{M_{feeding\ ICG}} \times 100\% \quad (2)$$

where $M_{loaded\ ICG}$ is the amount of ICG adsorbed by nHAP, M_{nHAP} is the total amount of nHAP, and $M_{feeding\ ICG}$ is the total amount of ICG.

2.4. Stability Characterization of SH-ICG/nHAP

The stability of SH-ICG/nHAP suspension was assessed in different physiological media and pH buffers, as well as for different times (up to 7 days). The physiological media investigated were pure water, saline, Dulbecco's Modified Eagle Medium (DMEM), and simulated body fluid (SBF). The concentrations of ICG in the supernatant obtained after their dissolution in different pH buffers (pH = 7.4, 6.5, 5.5) were tested.

2.5. Characterization of SH-ICG/nHAP

The crystal structure of the SH-ICG/nHAP was characterized by X-ray diffraction (XRD, D8 Advance, AXS). The chemical composition of the suspension was analyzed using Fourier transform infrared spectroscopy (FT-IR, Thermo Nicolet 6700, Waltham, MA, USA) and a UV–vis absorption spectrometer (UV-1900, SHIMADZU, Kyoto, Japan). The surface morphology of the nHAP and SH-ICG/nHAP were characterized using transmission electron microscopy (TEM, JEM-1400Plus, JEOL, Tokyo, Japan). The specific surface area of the SH-ICG/nHAP was characterized by a Brunner Emmet Teller surface area analyzer (BET, Micromeritics ASAP 2460, Norcross, GA, USA). The size of the nanoparticles was tested using a dynamic light scattering detector (DLS, Zetasizer Ultra, Malvern, UK).

2.6. PTT/PDT Effects of SH-ICG/nHAP

2.6.1. PTT Effect

The SH-ICG/nHAP suspension was placed in a centrifuge tube and irradiated under an 808 nm NIR laser. The power of the laser was regulated in the range of 0.5–1.5 W. The laser irradiation time was also adjustable. The temperature changes of the suspension were then recorded.

2.6.2. PDT Effect

The DPBF probe was used to characterize the PDT effect of the SH-ICG/nHAP suspension. First, the DPBF solution (5 mM) was prepared without light. Then, the SH-ICG/nHAP, ICG, and saline were added to the solution and the solution was irradiated under an NIR laser (1 W/cm^2, 8 min). Finally, the UV–vis absorption spectroscopy of the solution (416 nm) was recorded.

2.7. Photothermal Conversion Efficiency (η) of SH-ICG/nHAP

The η of SH-ICG/nHAP was evaluated based on a method reported in the literature [40].

$$\eta = hS(T_{max} - T_{surr}) - \frac{hS(T_{max} - T_{surr})}{I\left(1 - 10^{-A_{808}}\right)} \quad (3)$$

where h is the heat transfer coefficient, S is the surface area of the container, I is the laser power, T_{max} is the maximum steady state temperature, T_{surr} is the room temperature, and A_{808} is the absorbance value of the material at 808 nm.

τ_s could be obtained from the linear regression curve in the cooling curve. In this experiment, the τ_s is 279.72 s.

$$\tau_s = \frac{mc}{hS} \quad (4)$$

where m is the mass of the SH-ICG/nHAP suspension and c is the heat capacity of the SH-ICG/nHAP suspension, which is approximately the heat capacity of water, i.e., 4.2 J/(g·°C).

$$t = -\tau_s In\theta \quad (5)$$

$$\theta = \frac{T - T_{surr}}{T_{max} - T_{surr}} \quad (6)$$

2.8. Cell Culture, Cytotoxicity Assay, and Cell Ablation

2.8.1. Cell Culture

Normal human liver cells (HL7702 cells, Wuhan University of Technology, China) were cultured in 1640 medium supplemented with 10% fetal bovine serum (FBS) and 1% penicillin/streptomycin (PS). Human hepatocellular carcinoma cells (HepG2 cells, Wuhan University of Technology, China) were cultured in a high-glucose medium containing 10% FBS and 1% PS. The cells were incubated in a cell incubator (95% air, 5% CO_2, and 37 °C).

2.8.2. Cytotoxicity Assay

First, HL7702 cells were seeded in 96-well plates at a density of 5×10^3 cells/well. After 8 h, the old medium was replaced with a new medium. The new medium contained different concentrations of SH-ICG/nHAP. After 36 h, the old medium was removed, the CCK-8 solution was added, and the cells were incubated at 37 °C in the dark for 2 h. Next, the optical density (OD) value at 450 nm of the cells was measured, and the cell viability was calculated as follows:

$$Cell\ viability(\%) = \frac{A_1 - A_0}{A_c - A_0} \times 100\% \quad (7)$$

where A_0 is the OD value of the well without cells, A_1 is the OD value of the experimental group, and A_c is the OD value of the control group.

2.8.3. Cell Ablation

The experimental procedures were the same as the cytotoxicity experiments described above. After 24 h of co-culture, cells were irradiated under an 808 nm NIR laser. Parameters such as laser power density, time, and material concentrations were adjusted to explore the best treatment effect. Cell viability was measured using a CCK-8 assay.

2.9. Cell Uptake

The cell uptake of SH-ICG/nHAP was observed by TEM. The HepG2 cells were seeded and cultured in a culture bottle (95% air, 5% CO_2, and 37 °C). After 24 h, the medium was replaced with an SH-ICG/nHAP suspension diluted 10 times in fresh medium for the subsequent co-culture. The cells were washed three times with PBS after 12 h and were then fixed with 2.5% paraformaldehyde for 1 h at 4 °C. The cells were collected using a cell scraper. Finally, the cells were gradually dehydrated using ethanol before they were embedded and sliced for TEM observation.

2.10. In Vitro Detection of ROS

HepG2 cells and SH-ICG/nHAP were co-incubated for 12 h. After that, they were exposed to an 808 nm NIR laser (1 W/cm^2, 5 min) for irradiation. The cells were stained with DCFH-DA and left to incubate for 20 min. The cells were subsequently washed three times and observed using an inverted fluorescence microscope.

2.11. In Vivo PTT/PDT Effects

2.11.1. Establishment of Tumor Model

All experiments in this project were approved by the Institutional Animal Care and Use Committee of Wuhan University of Technology. HepG2 cells (2×10^6 cells in 0.1 mL PBS) were inoculated into the right armpit of 5-week-old female BALB/C nude mice (Weitong Lihua Company, Beijing, China). The length and width of the tumor were recorded using a Vernier caliper, and the tumor volume was calculated as follows:

$$Tumor\ volume\left(mm^3\right) = \frac{S^2 \times L}{2} \quad (8)$$

where S and L are the short and long diameters of the tumor. When the tumor volume of tumor-bearing mice reached 80–110 mm^3, the mice were grouped and treated.

2.11.2. PTT/PDT Effects

The tumor-bearing mice were divided into the saline, ICG, and SH-ICG/nHAP groups. Next, five mice were divided into one group. Different drugs were injected into the body through the tail vein. After 12 h, the tumor was irradiated with an 808 nm NIR laser at 0.9 W/cm^2 for 10 min, and the temperature changes in the tumor were recorded. The weights of the tumor-bearing mice and the tumor volumes were recorded every two days. Two weeks later, the tumor inhibitory effect of SH-ICG/nHAP and ICG were calculated.

2.12. Biosafety

In this study, 5% of fresh red blood cells was co-cultured with different materials (37 °C, 4 h). After that, the supernatant was centrifuged (1000 r/min, 5 min), and the OD value at 545 nm was measured. The hemolysis rate of the material was calculated as follows:

$$Hemolysis\ rate\ (\%) = \frac{A_1 - A_-}{A_+ - A_-} \times 100\% \quad (9)$$

where A_1, A_+, and A_- represent the OD value of the samples, positive control, and negative control, respectively.

After 14 days of treatment, blood samples were collected for routine blood tests and biochemical analyses. The tissues (heart, liver, spleen, lung, kidney, and tumor) of tumor-bearing mice were stained with H&E.

2.13. Statistical Analysis

All data were expressed as mean ± standard deviation (SD) and analyzed using Origin Lab, Microsoft Excel, and SPSS. One-way analysis of variance (ANOVA) was used to characterize the level of significant difference between the two groups, where * $p < 0.05$, ** $p < 0.01$, and *** $p < 0.001$.

3. Results and Discussion

3.1. Preparation and Characterization of SH-ICG/nHAP

3.1.1. Preparation of SH-ICG/nHAP

The synthesis method of SH-ICG/nHAP suspension is shown in Scheme 1. We used the hydrothermal method to synthesize nHAP carriers. The adsorption rate of the ICG, the ultrasonication time, and the amount of SH were explored.

At 2 h, the adsorption capacity of nHAP to ICG reached its maximum (Figure S1). In this study, the ICG and SH with the rich -O-SO_3- group were adsorbed on the surface of carriers to increase the steric repulsion and electric double layer repulsion of the nHAP, and the ultrasound-assisted method was used to disperse SH-ICG/nHAP. Therefore, the amount of SH and the ultrasonic time were further investigated to optimize the SH-ICG/nHAP preparation process. As the SH concentrations increased (Figure S2a), the size and polymer dispersity index (PDI) of the SH-ICG/nHAP suspension decreased, indicating its increased stability. An increasing amount of SH was adsorbed on the surface of nHAP, and the nHAP was dispersed by the repulsive force of SH. The best stability was achieved when the minimum concentration of SH was 0.4 mg/mL. The results also showed that the stability of SH-ICG/nHAP changed with the ultrasonic time (Figure S2b), and the best dispersion was achieved when the minimum ultrasonic time was 8 min. Based on the results of the above preparation process, a simple, rapid, and effective material preparation method was developed.

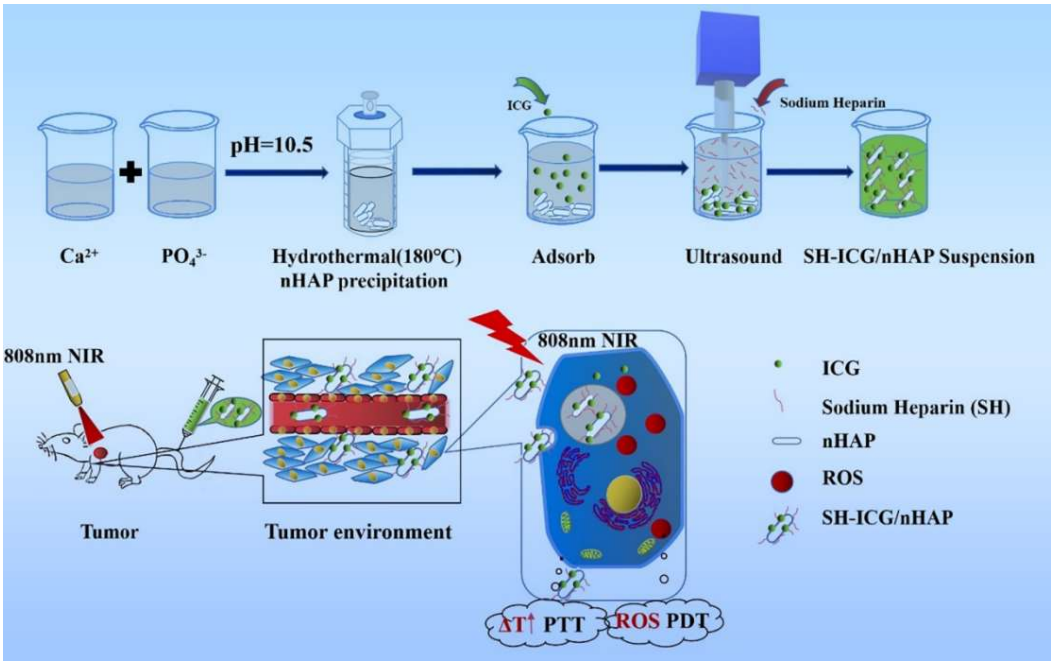

Scheme 1. The synthesis method and antitumor effect of SH-ICG/nHAP suspension.

3.1.2. Characterization of SH-ICG/nHAP

Figure 1a,b show the TEM images and size distribution statistics of nHAP and SH-ICG/nHAP. The images show that the synthesized nHAP (91.9 ± 1.7 nm × 28.0 ± 0.7 nm) had a rod-like morphology. However, ICG, absorption, and SH capping did not change its shape and size, and SH-ICG/nHAP still exhibited a rod-like morphology (90.2 ± 1.9 nm × 27.0 ± 0.5 nm). As shown in Figure S3, the surface area of the nHAP carrier was 43.8 m^2/g.

XRD results (Figure 1c) indicated that, despite introducing ICG and SH, the samples still had an nHAP crystal structure. SH-ICG/nHAP and nHAP had the same diffraction peaks (2θ = 25.92, 31.98, 34.04, 39.85, 46.81, and 49.63), which were attributed to the (002), (211), (112), (300), (310), (222), and (213) planes, respectively. FT-IR results (Figure 1d) demonstrated that SH and ICG were anchored on nHAP nanorods through the chemical bonding between the -O-SO_3- group of SH and Ca^{2+} on the surface of nHAP. For SH-ICG/nHAP, the characteristic vibrational bands of the OH– group (3570 cm^{-1}), PO_4^{3-} (562 cm^{-1}, 603 cm^{-1}, 1031 cm^{-1}), and CO_3^{2-} (1380–1580 cm^{-1}) indicated that the nHAP was synthesized successfully. Additionally, vibrations attributed to SH were observed in SH-ICG/nHAP. The S=O vibration of the -O-SO_3- group at 1236 cm^{-1}, the C-O vibration of the -COO- group at 1426 cm^{-1}, the C=O vibration of the -COO- group at 1633 cm^{-1}, and the C-H vibration of the -CH_3 group at 2950 cm^{-1}. Furthermore, unlike the SH molecule, the C-O vibration of the -COO- group and the S=O vibration of the -O-SO_3- group were shifted, indicating that the SH molecule was wrapped around the nHAP by the electrostatic interaction between the positively charged Ca^{2+} of SH-ICG/nHAP and the negatively charged -COO- and -O-SO_3- groups of SH. Thus, the agglomeration of nHAP was inhibited by the steric repulsion between SH molecules. Finally, the vibrations attributed to ICG were observed in SH-ICG/nHAP, which was a C=C vibration of ICG at 1090 cm^{-1}. This suggested the ICG was successfully loaded. In addition, ICG belongs to a -O-SO_3- group, and ICG can also be adsorbed on the surface of SH-ICG/nHAP through the -O-SO_3- group.

The UV–vis absorption spectrum of SH-ICG/HAP is shown in Figure 1e. The characteristic absorption peak of ICG is 780 nm. SH-ICG/nHAP also had a characteristic absorption peak at 708 nm. SH-ICG/HAP demonstrated a wide range of absorption peaks in the NIR region, indicating potential for PTT.

The ability of nHAP to adsorb ICG was tested, and it was found that the nHAP had a DLC of 13.3% for ICG, corresponding to a DLE of 88.6% (Figure 1f). This was because the surface area of the nHAP is certain, and as the concentrations of ICG increases, the adsorption of ICG by the carrier reaches a maximum.

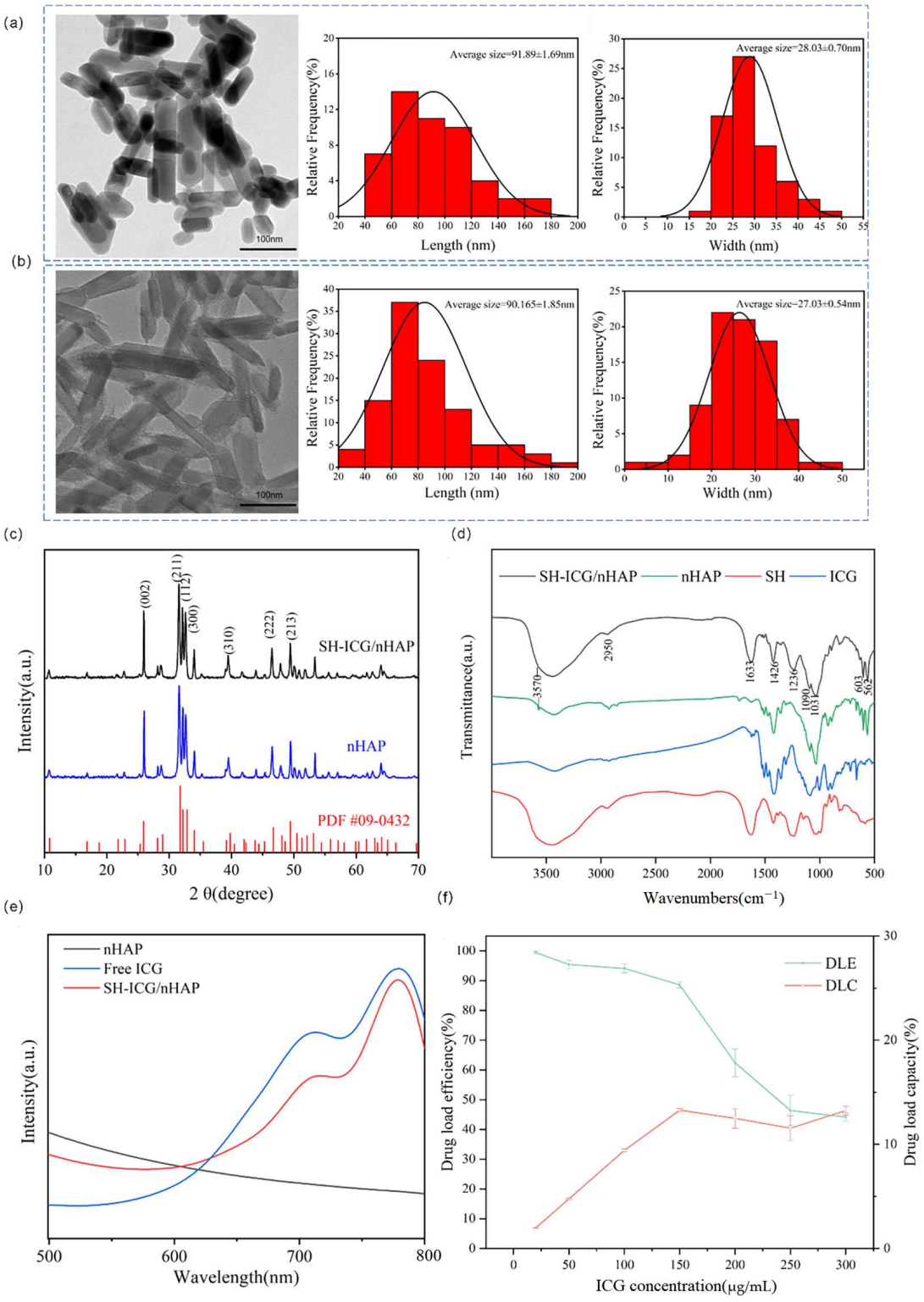

Figure 1. TEM images and size distribution statistics of (**a**) nHAP and (**b**) SH-ICG/nHAP (scale bar: 100 nm), (**c**) XRD of nHAP and SH-ICG/nHAPX, (**d**) FTIR spectra of nHAP, ICG, SH, and SH-ICG/nHAP, (**e**) UV–vis absorbance spectra of nHAP, free ICG, and SH-ICG/nHAP, and (**f**) DLE and DLC of nHAP.

3.1.3. Stability of SH-ICG/nHAP Suspension

To evaluate the stability of SH-ICG/nHAP *in vivo* and in tumor fluids with different pH environment, the release of ICG from SH-ICG/nHAP in different pH buffers was investigated for the first 24 h. The results (Figure 2a) show that SH-ICG/nHAP has good stability in acidic buffers (pH = 7.4, 6.5, and 5.5), and only a small amount of ICG was released. As the buffer pH decreased, the release of ICG increased. Ultimately, the release of ICG was 3.9 ± 0.1% at pH 7.4, 6.5 ± 0.2% at pH 6.5, and 7.9 ± 0.1% at pH 5.5. The nHAP has a high degree of crystallinity, resulting in stable physical and chemical properties in environments that are not very stimulating. The results also showed that ICG was not easily shed from the carrier in different body fluids and tumor sites, and demonstrated good stability. This effect greatly benefits the cycling stability of SH-ICG/nHAP in the body.

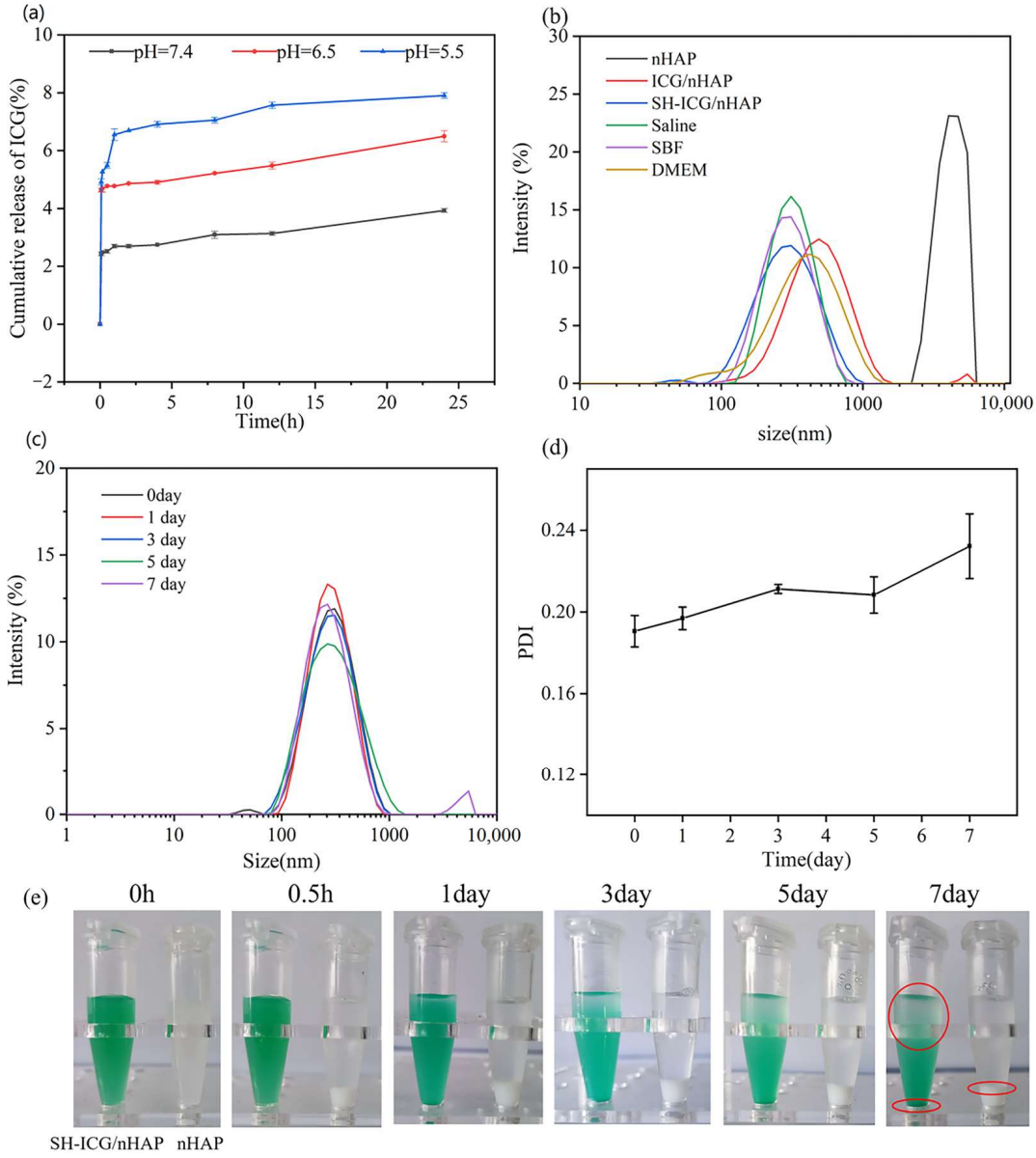

Figure 2. (**a**) Release of ICG in different pH buffer solutions (pH = 7.4, pH = 6.5, and pH = 5.5) at 24 h. (**b**) DLS of nHAP, ICG/nHAP, and SH-ICG/nHAP in different physiological media. (**c**) DLS of SH-ICG/nHAP at 7 days. (**d**) PDI of SH-ICG/nHAP at 7 days. (**e**) Photos of SH-ICG/nHAP at 7 days.

We used DLS to characterize the size and stability of the nHAP, ICG/nHAP, and SH-ICG/nHAP. As seen in Figure 2b, the size of the nHAP was 4 μm, and the stability

could be improved by adding a small amount of ICG. The agglomeration of nHAP could be further inhibited by adding a small amount of SH, reducing its size to 250 nm. The stability of SH-ICG/nHAP in different physiological media (saline, DMEM, and SBF) was explored. The results (Figure 2b) show that SH-ICG/nHAP has good stability in different systems, and its size was approximately 250 nm. We investigated the stability changes in the SH-ICG/nHAP suspension over the course of a week. According to the DLS results (Figure 2c), the average size of SH-ICG/nHAP particles in suspension is between 260 nm and 270 nm. A small number of particles had agglomerated at 7 days. The PDI results (Figure 2d) also show that PDI increases slowly over 7 days, indicating a decrease in stability. We also recorded optical photos of the SH-ICG/nHAP suspension and nHAP within a week. Figure 2e shows that the nHAP quickly agglomerates and settles within 0.5 h, while the SH-ICG/nHAP suspension only began to settle at 3 days, and one-third of it had settled at 7 days. The size analysis revealed a lack of obvious agglomeration; thus, settling may have occurred due to gravity. Therefore, the SH-ICG/nHAP suspension can greatly improve the stability of nHAP, inhibit its agglomeration, and provide a good solution for its *in vivo* application.

3.2. PTT/PDT Effects of SH-ICG/HAP

The photothermal conversion effect of SH-ICG/nHAP was investigated. The temperature of SH-ICG/HAP changed from 28 °C to 45 °C within 10 min under the NIR laser irradiation (0.5 W/cm^2); the temperature was maintained at 45 °C (Figure 3a). The critical temperature of cell ablation (42–45 °C) was exceeded. As the concentrations of ICG increased, so did the temperature. However, the temperature of the saline did not change. In addition, as the density of power increased (0.5–1.5 W/cm^2), the maximum temperature rose from 45 °C to 56 °C (Figure 3b), and the temperature changes of SH-ICG/nHAP showed a power dependence. Figure 3c shows the temperature changes of saline and SH-ICG/nHAP at different times measured by infrared imaging equipment. Figure 3d shows the temperature changes of SH-ICG/nHAP during an 808 nm NIR irradiation period (NIR on for 10 min, off for 10 min). The cooling time plot shows the negative natural logarithm of the driving force temperature (−ln θ) according to the temperature drop data of the SH-ICG/nHAP within 10 min of NIR closure (Figure 3e). According to the thermal time constant and related photothermal conversion efficiency formula, the η of SH-ICG/nHAP is 20.3%.

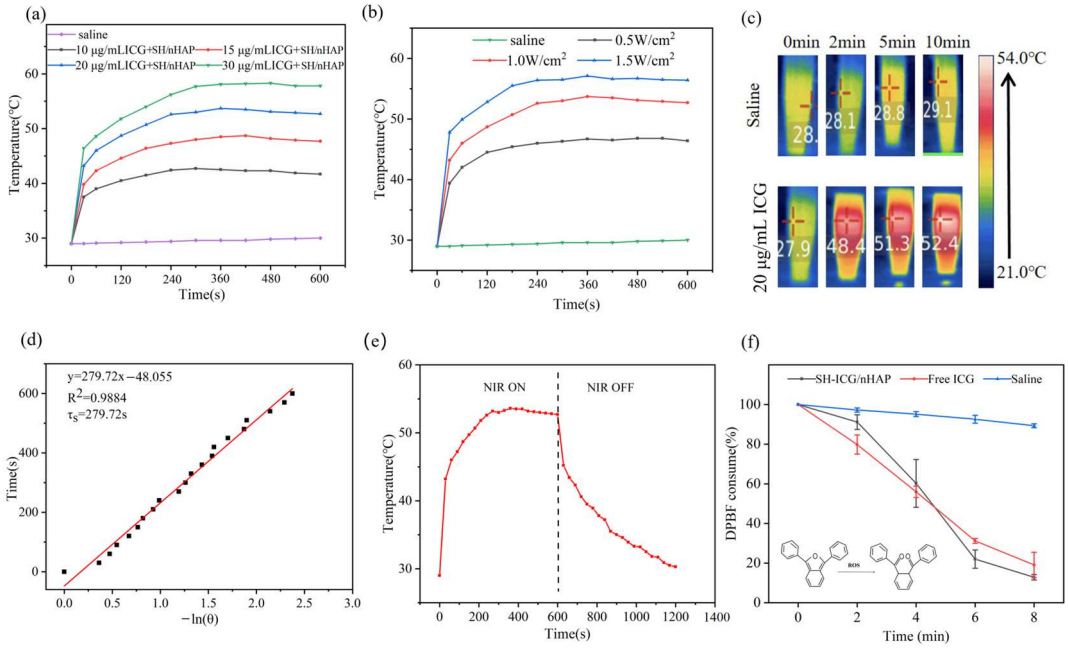

Figure 3. (**a**) Temperature changes in the SH−ICG/nHAP suspension with different samples under NIR laser irradiation for 10 min (1.0 W/cm^2). (**b**) Temperature changes in the SH-ICG/nHAP (20 μg/mL

ICG + SH/nHAP) suspension under NIR laser irradiation with different power densities. (**c**) NIR thermal images of saline and SH−ICG/nHAP. (**d**) "On/off" temperature changes in SH−ICG/nHAP under NIR laser irradiation. (**e**) Cooling time plot vs. negative natural logarithm of SH−ICG/nHAP. (**f**) Absorbance change in the DPBF probe solution at 416 nm under NIR laser irradiation.

DPBF is commonly used as a probe to detect ROS. In the presence of ROS, DPBF will be oxidized; thus, its UV–vis absorption peak at 416 nm will decrease. Under an NIR laser power density of 1.0 W/cm^2, we detected changes in the UV–vis absorption peak of SH-ICG/nHAP at 416 nm within 8 min (Figure 3f); thus, it can be inferred that SH-ICG/nHAP induces ROS production under an NIR laser. As the light time increased, the saline did not consume DPBF significantly. However, when the laser time was increased, the ROS levels of SH-ICG/nHAP and ICG became substantially elevated, thus consuming and oxidizing DPBF. At 8 min, 87.0% and 81.1% of the DPBF in the SH-ICG/nHAP and ICG solutions had been consumed, respectively. However, a small amount of ROS can cause great cytotoxicity. Therefore, SH-ICG/nHAP suspension can inhibit the growth of tumor cells by generating excessive ROS.

3.3. In Vitro Cytotoxicity, Hemolysis Rate, Cell Uptake, and Cell Ablation

The cell viability was quantified using a CCK-8 assay. HL7702 cells were co-cultured with different concentrations of SH-ICG/nHAP to detect the cytotoxicity (Figure 4a). When the concentrations of ICG were increased, SH-ICG/nHAP did not cause toxic damage to HL7702 cells; thus, SH-ICG/nHAP has good biocompatibility with normal cells. The drug injected through the tail vein first enters the blood; thus, it is important to evaluate the blood compatibility of a drug delivery system. Figure 4b shows that the hemolysis rates of the drug-loaded system at different concentrations were less than 5%.

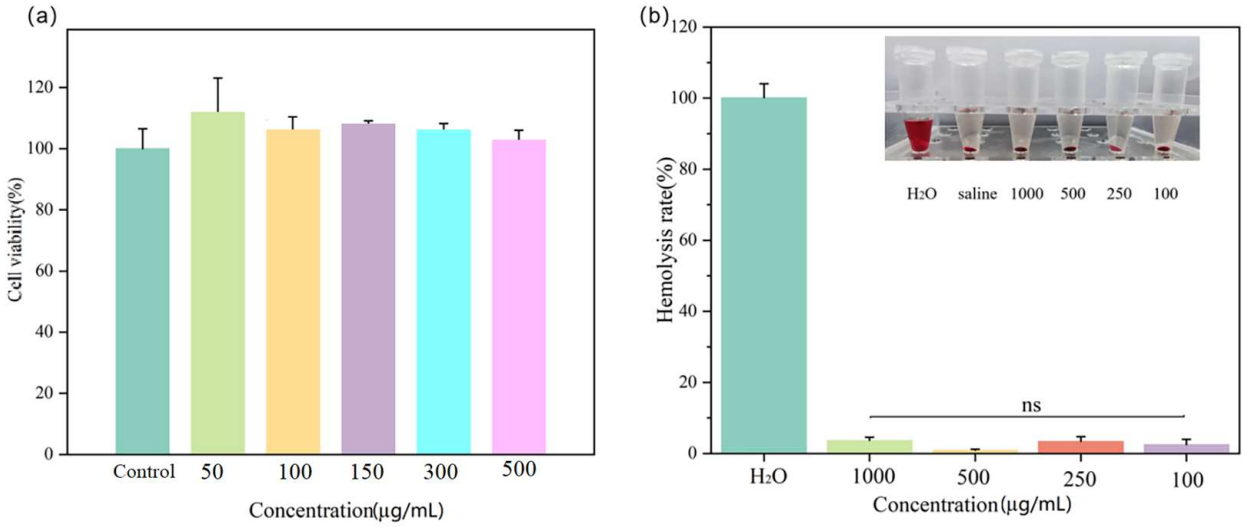

Figure 4. (**a**) The cell viability of HL7702 cells treated with different concentrations of SH-ICG/nHAP. (**b**) Hemolysis rate with different concentrations of SH-ICG/nHAP.

The TEM images reveal the presence of a large amount of material inside the cells after 12 h of co-culturing with SH-ICG/nHAP (Figure 5). This showed that the cells took up SH-ICG/nHAP within 12 h, meaning that the SH-ICG/nHAP could enter the cells to exert antitumor effects.

We evaluated the antitumor effect of SH-ICG/nHAP *in vitro*. A significant difference in cell viability before and after exposure to 808 nm NIR laser irradiation (0.8 W/cm^2, 5 min) was observed ($p < 0.01$). In addition, when the loading concentration of ICG was increased, the cell viability of HepG2 cells decreased from 48.5% to 21.4% (Figure 6a). This effect was due to the increased temperature and the production of excess ROS under

808 nm NIR laser irradiation. Tumor cells were damaged by high temperatures and ROS. HepG2 cells irradiated under an NIR laser were stained with Calcein-AM/PI and assessed under an inverted fluorescent microscope to characterize the cell viability (Figure 6d). Compared with the control group, the proportion of dead cells increased with the increase in ICG loading concentration, and the effect of inhibiting tumor cell proliferation became increasingly obvious. As shown in Figure 6b, with the increase in power density, the growth state of tumor cells also showed corresponding dependent changes. When the power density reached 1.5 W/cm^2, the viability of HepG2 cells was only 4.2%. Figure 6c shows that with an increased irradiation time, SH-ICG/nHAP produced more ROS and higher temperatures; thus, it increasingly inhibited tumor cell growth.

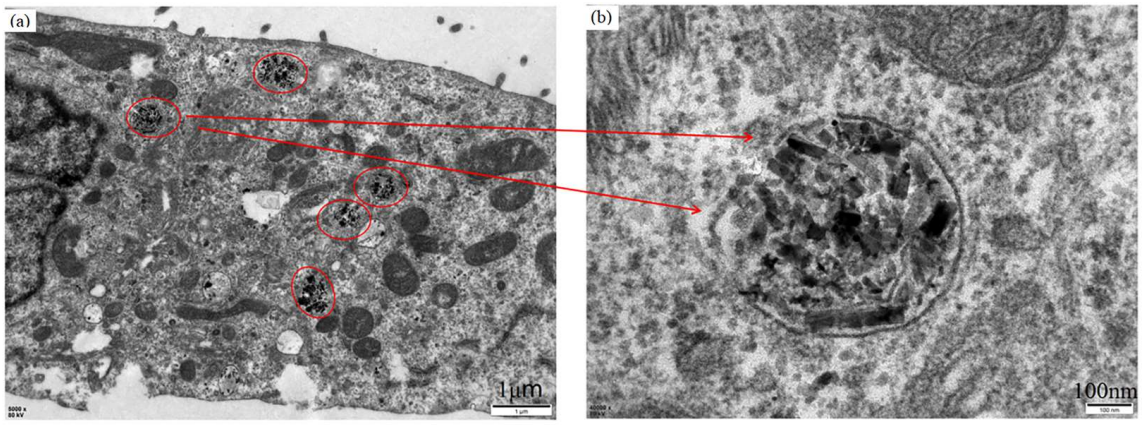

Figure 5. TEM images of HepG2 cells co-cultured with SH-ICG/nHAP for 12 h. (**a**) Scale bar: 1 μm. (**b**) Scale bar: 100 nm.

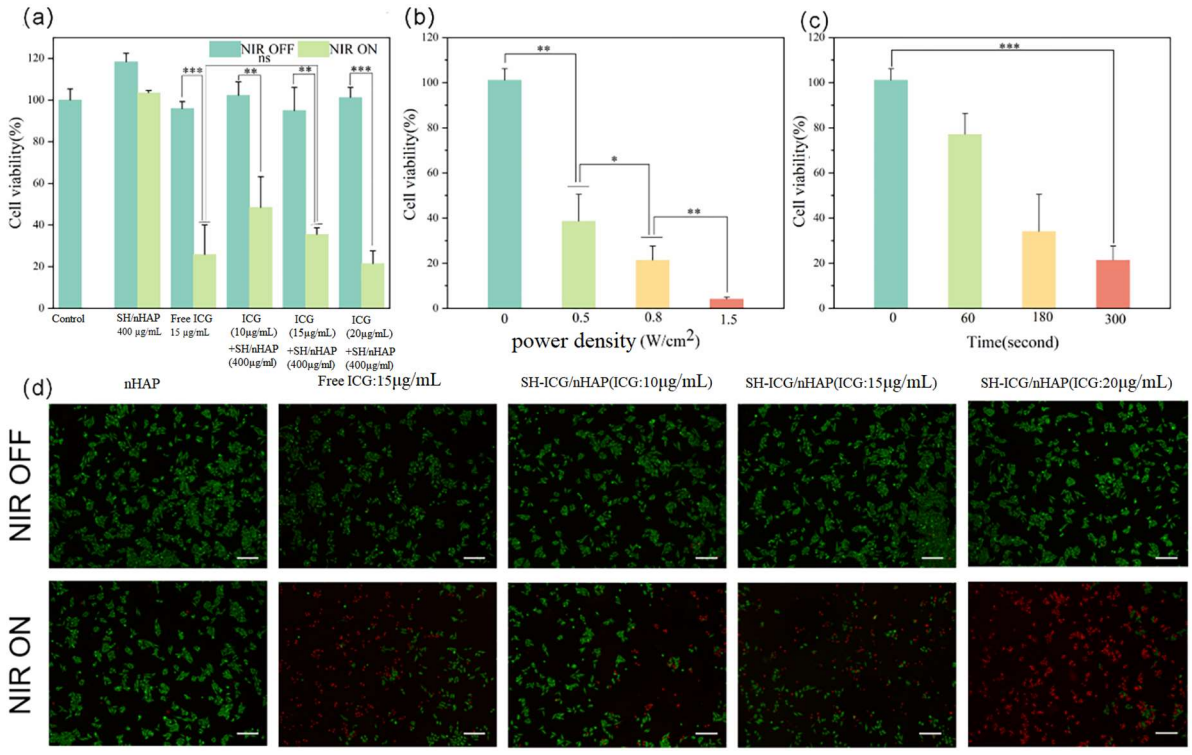

Figure 6. (**a**) The cell viability of HepG2 cells was co-cultured with different concentrations of samples, (**b**) different power densities, (**c**) and different times; (**d**) live/dead staining assay of HepG2 cells with different samples (scale bar: 200 μm) * $p < 0.05$, ** $p < 0.01$, and *** $p < 0.001$.

We used DCFH-DA to detect intracellular ROS. It can be seen from the results (Figure 7) that without 808 nm NIR laser irradiation, a small amount of ROS was produced in the cells in each group. After 808 nm NIR laser irradiation, there was no significant change in ROS levels in the control group. However, substantial ROS levels were detected in the ICG and SH-ICG/nHAP groups. This result indicated that cells uptake the material and produce ROS under NIR laser irradiation. Excessive ROS will damage the cells, achieving the goal of PDT.

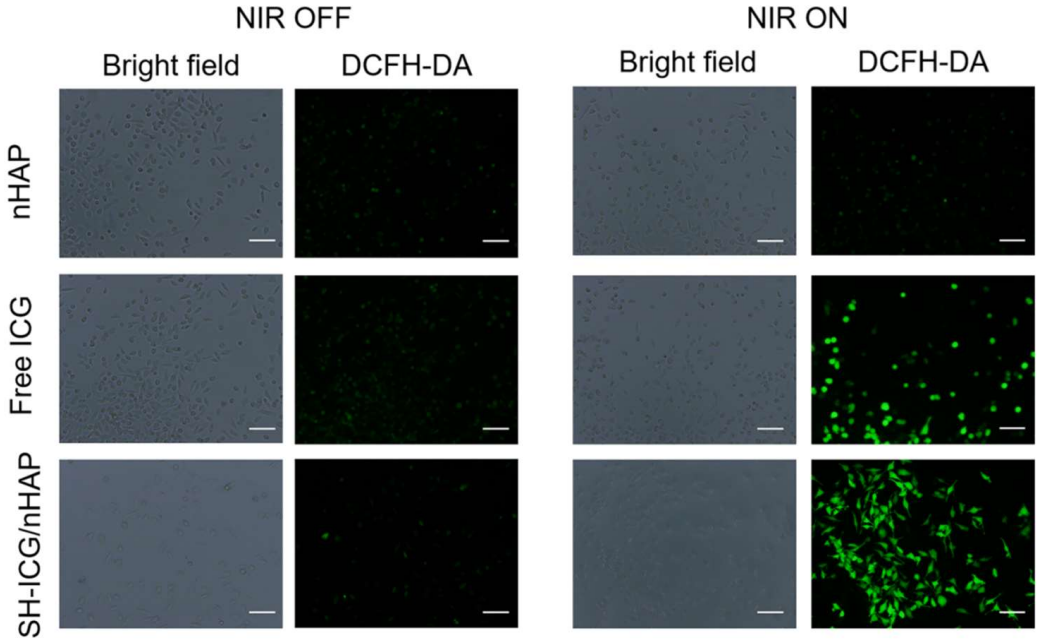

Figure 7. *In vitro* detection of ROS with free ICG and SH-ICG/nHAP (scale bar: 50 μm).

It can be seen from the above results that SH-ICG/nHAP is not cytotoxic to normal cells, and SH-ICG/nHAP has demonstrated good antitumor effect *in vitro*.

3.4. In Vivo PTT/PDT Antitumor Effects

Temperature measurements following laser irradiation at 808 nm were obtained 12 h after tail vein injection. The temperature changes at the tumor site after saline, free ICG, and SH-ICG/nHAP injections were recorded under an 808 nm NIR laser (Figure 8a,b). A small increase in temperature was seen in the saline group (control), which was maintained at approximately 39 °C. The temperature of the ICG group could be raised to approximately 43 °C. However, the temperature of group SH-ICG/nHAP increased significantly to 45 °C in 5 min and was maintained at 47–50 °C for a long time. This increase in temperature at the tumor site also demonstrates that SH-ICG/nHAP can improve the accumulation of ICG at the tumor site. Mice tumor volume and weight were recorded over the course of 14 days (Figure 8c,d). In the control group (Figure 8e), the tumor grew rapidly, and the volume and weight reached 817.1 mm^3 and 1170.9 mg after 14 days. In the ICG group, the tumor volume and weight reached 665.4 mm^3 and 1012.0 mg after 14 days, and the tumor inhibition ability was 13.57%, indicating the poor inhibition of tumor growth. However, the tumor growth of the SH-ICG/nHAP group was slow; the tumor volume and weight reached 316.4 mm^3 and 351.9 mg after 14 days, and the tumor inhibition ability was 69.94% (Figure 8f). The results of H&E staining (Figure 8g) of the tumors showed that most of the tumor cells in the SH-ICG/nHAP group were damaged; thus, the growth state of the tumor site was greatly reduced. The above animal experimental results indicated that SH-ICG/nHAP achieved the goal of PTT/PDT *in vivo*.

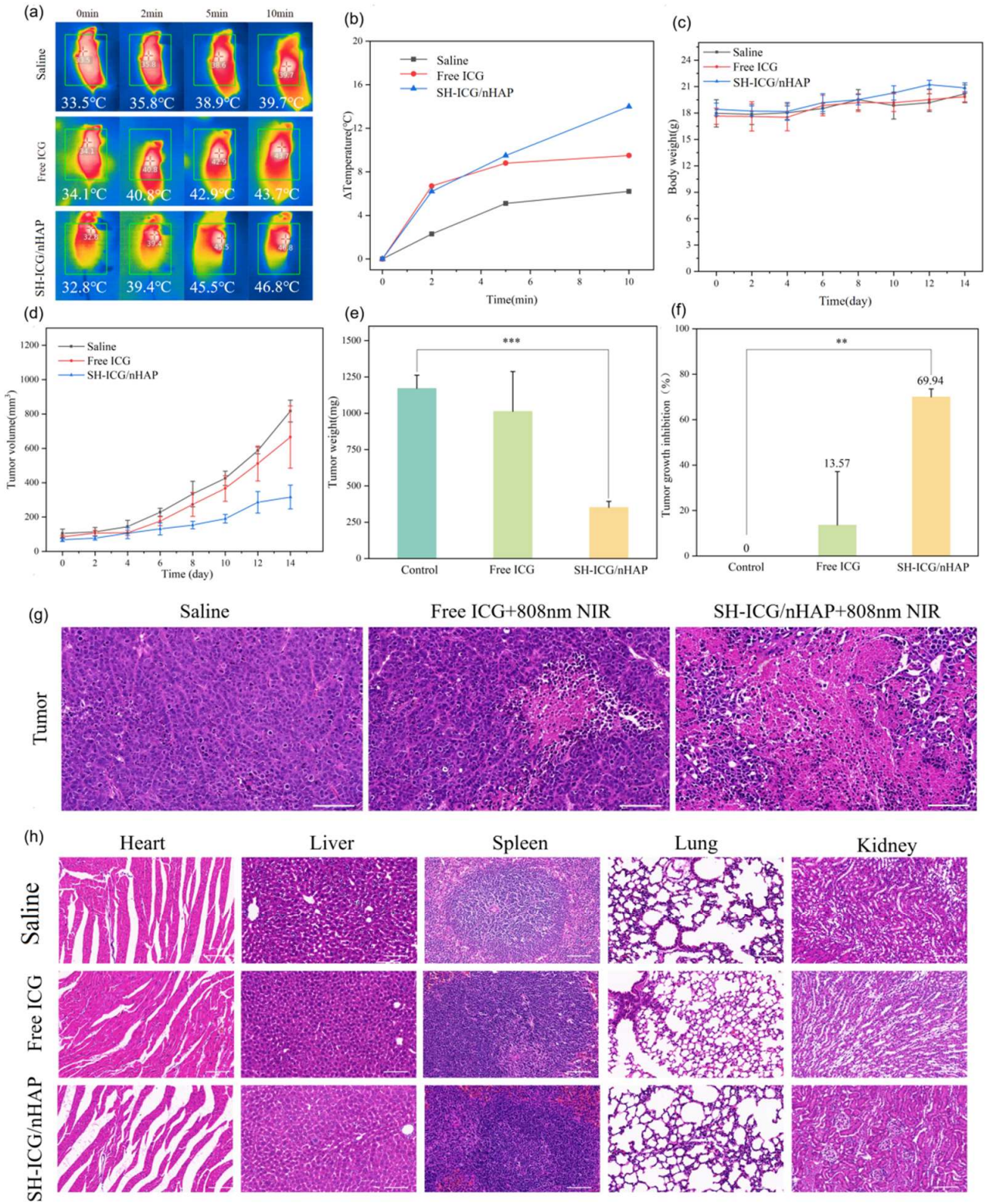

Figure 8. (**a**) Mice thermal images and (**b**) tumor temperature changes were recorded during treatment, (**c**) body weight changes, (**d**) tumor volume changes in tumor-bearing mice two weeks after treatment, (**e**) tumor weight of mice after 14 days, (**f**) tumor growth inhibition of the control, free ICG, and SH-ICG/nHAP groups, (**g**) H&E staining images of tumor regions in different groups (scale bar: 50 μm), (**h**) H&E staining images of major organs (heart, liver, spleen, lung, and kidney) in different groups (scale bar: 50 μm) * $p < 0.05$, ** $p < 0.01$, and *** $p < 0.001$.

We evaluated the biosafety of SH-ICG/nHAP *in vivo*. Biochemical parameters in the blood can be used to assess tissue function. For example, alanine aminotransferase (ALT) and aspartate aminotransferase (AST) can be used to evaluate liver function, and creatinine (CREA) can be used to evaluate kidney function. As can be seen in Figure S4, the biochemical indices of the blood did not show any abnormalities compared with the control group 14 days after the drug was injected into the tail vein, and it did not affect liver and kidney function. In addition, the blood routine examination showed that SH-ICG/nHAP did not cause an inflammatory response *in vivo* (Figure S5). Furthermore, the H&E-stained slices (heart, liver, spleen, lung, and kidney) revealed that each tissue was normal, and there was no inflammation or other toxic effect (Figure 8h). Therefore, SH-ICG/nHAP is a good biocompatible drug delivery system.

4. Conclusions

In summary, the SH-ICG/nHAP suspension was successfully prepared using the ultrasound-assisted hydrothermal method through the combined effect of ultrasound and SH. Short rod-shaped nHAP carriers have good crystallinity. The nHAP has a DLC of 13.3% for ICG, corresponding to a DLE of 88.6%. The SH-ICG/nHAP suspension is very stable in different media and acidic environments and maintains good stability over time (7 days). Additionally, the release of ICG is 3.9 $\pm$ 0.1% at pH 7.4, 6.5 $\pm$ 0.2% at pH 6.5, and 7.9 $\pm$ 0.1% at pH 5.5. The SH-ICG/nHAP suspension has good PDT/PTT effects. Under the irradiation of an 808 nm NIR laser at 0.8 W/cm^2 for 5 min, SH-ICG/nHAP was found to significantly inhibit HepG2 cells proliferation (78.58%), similar to free ICG. The inhibition rate of tumor growth *in vivo* is 69.94%. The prepared SH-ICG/nHAP suspension has good biosafety and can be used for combined tumor therapy *in vitro* and *in vivo*. In conclusion, this study provides a simple and effective method for the preparation of stable nHAP suspensions, which can help promote the application of nHAP as a drug carrier *in vivo*. SH-ICG/nHAP is expected to be a drug delivery system for combined tumor therapy.

Supplementary Materials: The following supporting information can be downloaded at: https://www.mdpi.com/article/10.3390/cryst13091387/s1, Figure S1: Changes in the adsorption capacity of ICG with the adsorption time; Figure S2: Different parameters (SH concentration (a) and ultrasonic time (b)), the PDI and the size of SH-ICG/nHAP are shown; Figure S3: N2 adsorption-desorption of nHAP; Figure S4: Blood biochemistry analysis (ALT, AST, and CREA) of tumor-bearing mice in different groups; Figure S5: Blood analysis of tumor-bearing mice in different groups.

Author Contributions: Conceptualization, Q.S. and Y.H.; formal analysis, Y.F. and X.T.; funding acquisition, Y.H.; methodology, Q.S., Z.-Y.D., and Y.H.; software, C.L.; supervision, Y.H.; validation, Y.F.; writing—original draft, Q.S.; writing—review and editing, Q.S. and Y.H. All authors have read and agreed to the published version of the manuscript.

Funding: This work was supported by the National Natural Science Foundation of China (51672206), the Fundamental Research Funds for the Central Universities (WUT: 2022IVB003).

Institutional Review Board Statement: The study was conducted in accordance with the Declaration of Helsinki, and approved by the Institutional Review Board of Wuhan University of Technology (WHUT (Animal ethics) NO 2023-19, 8 March 2023).

Data Availability Statement: The data presented in this study are available upon request from the corresponding author.

Acknowledgments: The authors acknowledge the financial support of the National Natural Science Foundation of China, the Fundamental Research Funds for the Central Universities.

Conflicts of Interest: The authors declare that they have no conflicts of interest.

References

1. Ji, C.; Yuan, A.; Xu, L.; Zhang, F.; Zhang, S.; Zhao, X.; Liu, G.; Chen, W.; Guo, H. Activatable Photodynamic Therapy for Prostate Cancer by NIR Dye/Photosensitizer Loaded Albumin Nanoparticles. *J. Biomed. Nanotechnol.* **2019**, *15*, 311–318. [CrossRef]
2. Han, Y.H.; Kankala, R.K.; Wang, S.B.; Chen, A.Z. Leveraging Engineering of Indocyanine Green-Encapsulated Polymeric Nanocomposites for Biomedical Applications. *Nanomaterials* **2018**, *8*, 360. [CrossRef]
3. Capozza, M.; Blasi, F.; Valbusa, G.; Oliva, P.; Cabella, C.; Buonsanti, F.; Cordaro, A.; Pizzuto, L.; Maiocchi, A.; Poggi, L. Photoacoustic imaging of integrin-overexpressing tumors using a novel ICG-based contrast agent in mice. *Photoacoustics* **2018**, *11*, 36–45. [CrossRef]
4. Jia, D.; Liu, H.; Zheng, S.; Yuan, D.; Sun, R.; Wang, F.; Li, Y.; Li, H.; Yuan, F.; Fan, Q.; et al. ICG-Dimeric Her2-Specific Affibody Conjugates for Tumor Imaging and Photothermal Therapy for Her2-Positive Tumors. *Mol. Pharm.* **2023**, *20*, 427–437. [CrossRef]
5. Ashokan, A.; Gowd, G.S.; Somasundaram, V.H.; Bhupathi, A.; Peethambaran, R.; Unni, A.K.; Palaniswamy, S.; Nair, S.V.; Koyakutty, M. Multifunctional calcium phosphate nano-contrast agent for combined nuclear, magnetic and near-infrared *in vivo* imaging. *Biomaterials* **2013**, *34*, 7143–7157. [CrossRef]
6. Barnes, K.D.; Shafirstein, G.; Webber, J.S.; Koonce, N.A.; Harris, Z.; Griffin, R.J. Hyperthermia-enhanced indocyanine green delivery for laser-induced thermal ablation of carcinomas. *Int. J. Hyperth.* **2013**, *29*, 474–479. [CrossRef]
7. Kadkhoda, J.; Tarighatnia, A.; Barar, J.; Aghanejad, A.; Davaran, S. Recent advances and trends in nanoparticles based photothermal and photodynamic therapy. *Photodiagn. Photodyn. Ther.* **2022**, *37*, 102697. [CrossRef]
8. Gao, F.; Jiang, L.; Zhang, J.; Chang, Y.; Gao, W.; Ding, L.; Ma, G.; Ma, X.; Guo, Y. Near-Infrared Light-Responsive Nanosystem with Prolonged Circulation and Enhanced Penetration for Increased Photothermal and Photodynamic Therapy. *ACS Mater. Lett.* **2022**, *5*, 1–10. [CrossRef]
9. Sun, D.; Huang, Y.; Zhang, X.; Peng, J.; Li, J.; Ming, J.; Wei, J.; Chen, X.; Zheng, N. A Pd corolla-human serum albumin-indocyanine green nanocomposite for photothermal/photodynamic combination therapy of cancer. *J. Mater. Chem. B* **2018**, *6*, 6969–6976. [CrossRef]
10. Cai, W.; Gao, H.; Chu, C.; Wang, X.; Wang, J.; Zhang, P.; Lin, G.; Li, W.; Liu, G.; Chen, X. Engineering Phototheranostic Nanoscale Metal-Organic Frameworks for Multimodal Imaging-Guided Cancer Therapy. *ACS Appl. Mater. Interfaces* **2017**, *9*, 2040–2051. [CrossRef]
11. Hu, X.; Li, J.; Chen, Y.; Long, Q.; Bai, Y.; Li, R.; Wang, K.; Jiang, M.; Chen, C.; Mao, J.; et al. A Self-Assembly ICG Nanoparticle Potentiating Targeted Photothermal and Photodynamic Therapy in NSCLC. *ACS Biomater. Sci. Eng.* **2022**, *8*, 4535–4546. [CrossRef]
12. Cai, L.; Sheng, Z.; Hu, D.; Xue, M.; He, M.; Gong, P. Indocyanine Green Nanoparticles for Theranostic Applications. *Nano-Micro Lett.* **2013**, *5*, 145–150. [CrossRef]
13. Wang, H.; Li, X.; Tse, B.W.; Yang, H.; Thorling, C.A.; Liu, Y.; Touraud, M.; Chouane, J.B.; Liu, X.; Roberts, M.S.; et al. Indocyanine green-incorporating nanoparticles for cancer theranostics. *Theranostics* **2018**, *8*, 1227–1242. [CrossRef]
14. Yu, C.; Liu, C.; Wang, S.; Li, Z.; Hu, H.; Wan, Y.; Yang, X. Hydroxyethyl Starch-Based Nanoparticles Featured with Redox-Sensitivity and Chemo-Photothermal Therapy for Synergized Tumor Eradication. *Cancers* **2019**, *11*, 207. [CrossRef]
15. Zheng, X.; Xing, D.; Zhou, F.; Wu, B.; Chen, W.R. Indocyanine green-containing nanostructure as near infrared dual-functional targeting probes for optical imaging and photothermal therapy. *Mol. Pharm.* **2011**, *8*, 447–456. [CrossRef]
16. Yu, L.; Dong, A.; Guo, R.; Yang, M.; Deng, L.; Zhang, J. DOX/ICG Coencapsulated Liposome-Coated Thermosensitive Nanogels for NIR-Triggered Simultaneous Drug Release and Photothermal Effect. *ACS Biomater. Sci. Eng.* **2018**, *4*, 2424–2434. [CrossRef]
17. Wang, G.; Zhang, F.; Tian, R.; Zhang, L.; Fu, G.; Yang, L.; Zhu, L. Nanotubes-Embedded Indocyanine Green-Hyaluronic Acid Nanoparticles for Photoacoustic-Imaging-Guided Phototherapy. *ACS Appl. Mater. Interfaces* **2016**, *8*, 5608–5617. [CrossRef]
18. Vivek, R.; Thangam, R.; NipunBabu, V.; Rejeeth, C.; Sivasubramanian, S.; Gunasekaran, P.; Muthuchelian, K.; Kannan, S. Multifunctional HER2-antibody conjugated polymeric nanocarrier-based drug delivery system for multi-drug-resistant breast cancer therapy. *ACS Appl. Mater. Interfaces* **2014**, *6*, 6469–6480. [CrossRef]
19. Wu, L.; Fang, S.; Shi, S.; Deng, J.; Liu, B.; Cai, L. Hybrid polypeptide micelles loading indocyanine green for tumor imaging and photothermal effect study. *Biomacromolecules* **2013**, *14*, 3027–3033. [CrossRef]
20. Kim, T.H.; Chen, Y.; Mount, C.W.; Gombotz, W.R.; Li, X.; Pun, S.H. Evaluation of temperature-sensitive, indocyanine green-encapsulating micelles for noninvasive near-infrared tumor imaging. *Pharm. Res.* **2010**, *27*, 1900–1913. [CrossRef]
21. Ma, Y.; Liu, X.; Ma, Q.; Liu, Y. Near-infrared nanoparticles based on indocyanine green-conjugated albumin: A versatile platform for imaging-guided synergistic tumor chemo-phototherapy with temperature-responsive drug release. *Onco Targets Ther.* **2018**, *11*, 8517–8528. [CrossRef]
22. Zhang, M.; Zhang, L.; Chen, Y.; Li, L.; Su, Z.; Wang, C. Precise synthesis of unique polydopamine/mesoporous calcium phosphate hollow Janus nanoparticles for imaging-guided chemo-photothermal synergistic therapy. *Chem. Sci.* **2017**, *8*, 8067–8077. [CrossRef]
23. Miranda, D.; Wan, C.; Kilian, H.I.; Mabrouk, M.T.; Zhou, Y.; Jin, H.; Lovell, J.F. Indocyanine green binds to DOTAP liposomes for enhanced optical properties and tumor photoablation. *Biomater. Sci.* **2019**, *7*, 3158–3164. [CrossRef]
24. Guerrini, L.; Jurasekova, Z.; del Puerto, E.; Hartsuiker, L.; Domingo, C.; Garcia-Ramos, J.V.; Otto, C.; Sanchez-Cortes, S. Effect of metal-liquid interface composition on the adsorption of a cyanine dye onto gold nanoparticles. *Langmuir* **2013**, *29*, 1139–1147. [CrossRef]
25. Zhu, L.; Yang, Y.; Li, X.; Zheng, Y.; Li, Z.; Chen, H.; Gao, Y. Facile preparation of indocyanine green and tiny gold nanoclusters co-loaded nanocapsules for targeted synergistic sono-/photo-therapy. *J. Colloid. Interface Sci.* **2022**, *627*, 596–609. [CrossRef]

26. Chen, Y.; Wang, X.; Lu, Z.; Chang, C.; Zhang, Y.; Li, Y.; Yi, M.; Xiong, B.; Lu, B. Lactobionic acid-functionalized hollow mesoporous silica nanoparticles for cancer chemotherapy and phototherapy. *Process Biochem.* **2022**, *121*, 698–706. [CrossRef]
27. Rao, K.M.; Parambadath, S.; Kumar, A.; Ha, C.S.; Han, S.S. Tunable Intracellular Degradable Periodic Mesoporous Organosilica Hybrid Nanoparticles for Doxorubicin Drug Delivery in Cancer Cells. *ACS Biomater. Sci. Eng.* **2018**, *4*, 175–183. [CrossRef]
28. Hong, E.J.; Sivakumar, P.; Ravichandran, V.; Choi, D.G.; Kim, Y.S.; Shim, M.S. Pro-Oxidant Drug-Loaded Au/ZnO Hybrid Nanoparticles for Cancer-Specific Chemo-Photodynamic Combination Therapy. *ACS Biomater. Sci. Eng.* **2019**, *5*, 5209–5217. [CrossRef]
29. Syamchand, S.S.; Sony, G. Multifunctional hydroxyapatite nanoparticles for drug delivery and multimodal molecular imaging. *Microchim. Acta* **2015**, *182*, 1567–1589. [CrossRef]
30. Lin, K.; Xia, L.; Gan, J.; Zhang, Z.; Chen, H.; Jiang, X.; Chang, J. Tailoring the nanostructured surfaces of hydroxyapatite bioceramics to promote protein adsorption, osteoblast growth, and osteogenic differentiation. *ACS Appl. Mater. Interfaces* **2013**, *5*, 8008–8017. [CrossRef] [PubMed]
31. Li, F.; Xing, Q.; Han, Y.; Li, Y.; Wang, W.; Perera, T.S.H.; Dai, H. Ultrasonically assisted preparation of poly(acrylic acid)/calcium phosphate hybrid nanogels as pH-responsive drug carriers. *Mater. Sci. Eng. C Mater. Biol. Appl.* **2017**, *80*, 688–697. [CrossRef] [PubMed]
32. Khan, M.A.; Wu, V.M.; Ghosh, S.; Uskokovic, V. Gene delivery using calcium phosphate nanoparticles: Optimization of the transfection process and the effects of citrate and poly(l-lysine) as additives. *J. Colloid. Interface Sci.* **2016**, *471*, 48–58. [CrossRef]
33. Li, D.; Huang, X.; Wu, Y.; Li, J.; Cheng, W.; He, J.; Tian, H.; Huang, Y. Preparation of pH-responsive mesoporous hydroxyapatite nanoparticles for intracellular controlled release of an anticancer drug. *Biomater. Sci.* **2016**, *4*, 272–280. [CrossRef]
34. Han, Y.; Li, S.; Cao, X.; Yuan, L.; Wang, Y.; Yin, Y.; Qiu, T.; Dai, H.; Wang, X. Different inhibitory effect and mechanism of hydroxyapatite nanoparticles on normal cells and cancer cells *in vitro* and *in vivo*. *Sci. Rep.* **2014**, *4*, 7134. [CrossRef]
35. Wang, Y.C.; Dai, H.L.; Li, Z.H.; Meng, Z.Y.; Xiao, Y.; Zhao, Z. Mesoporous polydopamine-coated hydroxyapatite nano-composites for ROS-triggered nitric oxide-enhanced photothermal therapy of osteosarcoma. *J. Mater. Chem. B* **2021**, *9*, 7401–7408. [CrossRef]
36. Mushtaq, A.; Tang, Z.; Hou, Y.; Zhu, Z.; Tian, C.; Wu, Y.; Lu, Y.; Iqbal, M.Z.; Kong, X. Biocompatible magnetic hydroxyapatite Fe3O4-HAp nanocomposites for T1-magnetic resonance imaging guided photothermal therapy of breast cancer. *Mater. Today Commun.* **2022**, *31*, 103734. [CrossRef]
37. Cheng, X.; Xu, Y.; Zhang, Y.; Jia, C.; Wei, B.; Hu, T.; Tang, R.; Li, C. Glucose-Targeted Hydroxyapatite/Indocyanine Green Hybrid Nanoparticles for Collaborative Tumor Therapy. *ACS Appl. Mater. Interfaces* **2021**, *13*, 37665–37679. [CrossRef]
38. Zhang, G.; Lu, Y.; Song, J.; Huang, D.; An, M.; Chen, W.; Han, P.; Yao, X.; Zhang, X. A multifunctional nano-hydroxyapatite/MXene scaffold for the photothermal/dynamic treatment of bone tumours and simultaneous tissue regeneration. *J. Colloid Interface Sci.* **2023**, *652*, 1673–1684. [CrossRef]
39. Xing, Q.; Zhang, X.; Wu, D.; Han, Y.; Nirmali Wickramaratne, M.; Dai, H.; Wang, X. Ultrasound-Assisted Synthesis and Characterization of Heparin-Coated Eu3+ Doped Hydroxyapatite Luminescent Nanoparticles. *Colloid Interface Sci. Commun.* **2019**, *29*, 17–25. [CrossRef]
40. Xi, D.; Xiao, M.; Cao, J.; Zhao, L.; Xu, N.; Long, S.; Fan, J.; Shao, K.; Sun, W.; Yan, X.; et al. NIR Light-Driving Barrier-Free Group Rotation in Nanoparticles with an 88.3% Photothermal Conversion Efficiency for Photothermal Therapy. *Adv. Mater.* **2020**, *32*, e1907855. [CrossRef]